Essential Readings in Light Metals: Aluminum Reduction Technology.
Edited by Geoff Bearne, Marc Dupuis and Gary Tarcy.

COUPLED CURRENT DISTRIBUTION AND CONVECTION SIMULATOR FOR ELECTROLYSIS CELLS

Knut Bech, Stein T. Johansen , Asbjørn Solheim, and Torstein Haarberg

SINTEF Materials Technology, N – 7465 Trondheim, Norway

Abstract

A simulator for coupled current distribution and convection in electrolysis cells has been developed. The simulator solves the electric and temperature fields in the electrolyte, electrodes and surrounding solids, as well as the rate of anodic gas evolution and the resulting convection in the electrolyte. The simulator is based on the computational fluid dynamics software Fluent 4.5, to which we have added a solver for the electric field including electrochemical overvoltage. The surface potential model is based on an iterative flux method. Furthermore, the amount of gas released from the anode is a function of the local current density. The resulting gas induced convection depends on gas mass flow and bubble size. The local electric conductivity of the electrolyte is a function of the local gas fraction. Calculations have been performed for various cell geometries with both horizontal and vertical electrodes. Effects of bubble size and cell geometry have been studied. The physical parameters were chosen to match those encountered in aluminium electrolysis, but the simulator is general and can be applied to all kinds of electrolysis cells. Additional calculations of side ledge heat transfer in Søderberg- and prebake-cells are presented and compared with measurements.

Introduction

Computational fluid dynamics (CFD) and electrochemistry are important tools for the design of the next generation of electrolysis cells. By testing various geometries and electrode configurations in the computer, the design can be refined before building a laboratory cell. Simulations might be even more important when doing the scale-up from laboratory to pilot scale, and further up to production scale. Detailed physical phenomena, such as the static deformation of the bath/metal interface due to gas-induced convection, can be studied by applying CFD [8].

In electrolysis cells, a variety of physical phenomena must be modeled simultaneously. These includes primary and secondary current distribution, gas release and bubbly flow, bath convection, effects on electrical conductivity, temperature and temperature-dependent properties such as density and viscosity. The large number of equations to be solved and coupled in an application-specific way, calls for the use of existing software in combination with new models. To build a simulator from scratch will require several years of work. We have chosen to add a solver for the electromagnetic field to one of the world's leading CFD codes, Fluent [3]. Thereby, we can concentrate on issues of great importance for electrolysis, such as secondary current distribution and bubble-driven flow.

The present paper presents a model for secondary current distribution in the finite-volume framework. The model has been implemented, together with the electromagnetic field, as an integral part of a general purpose CFD code. Simulation results concerning the heat transfer coefficients at the side-ledge in two different traditional Hall-Heroult cells is shown, as well as the current and hydrodynamic flow fields in an aluminum reduction cell with vertical inert electrodes.

Theory

Electrochemical Overvoltage Model

The current continuity equation under steady-state conditions can be formulated

$$\vec{\nabla} \cdot \vec{j} = \vec{\nabla} \cdot \left(\sigma \vec{U} \times \vec{B} - \sigma \vec{\nabla} \phi \right) = 0 \qquad (1)$$

where j is the current density [A/m^2], σ is the electrical conductivity [S/m], U is the bath velocity [m/s], B is the magnetic field [T] and ϕ is the electric potential [V]. Equation (1) is solved numerically applying the finite-volume formulation[1]. Neumann (specified current density j) or Dirichlet (specified potential) type conditions are given at the boundaries or internal electrodes. Three different types of surface potentials ϕ_s [V] are considered here: 1)

Reversible voltage, 2) Activation overvoltage (described by a Tafel equation), and 3) Concentration overvoltage. The reversible voltage is independent of the current density.

Reversible voltage: $\phi_s = const.$ (2)

Activation overvoltage: $\phi_s = \eta_a = a + b \log j_a$ (3)

Concentration overvoltage: $\phi_s = |\eta_c| \approx b_c \frac{j_c \varepsilon}{k_c}$ (4)

where a and b are Tafel coefficients, b_c is a constant [Vm/As], ε is the current efficiency (given as a fraction, *e.g.*, $\varepsilon = 0.95$), and k_c is the mass transfer coefficient for AlF_3 at the cathode. The subscripts refer to anode (a) and cathode (c). In the equation for the cathodic concentration overvoltage (4), it was assumed that the current density is far below the limiting current density.

In principle, all types of equations can be used for calculating surface potentials. Eqs. (3) and (4) are the common choices for Hall-Heroult cells[17], and we have chosen to apply these equations when calculating the electric field in the example with vertical, inert electrodes.

The mass transfer coefficient at the cathode was calculated from [4]

$$\frac{k_c}{u_\tau} = 0.108 Sc^{-0.5} \quad (5)$$

where u_τ is the velocity based on shear stress on the cathode from the bath and the Schmidt number is approximately 130 [5,6] in cryolite melts.

Surface Potentials - Calculation of Effective Conductivity

The problem of surface potentials (overvoltage and reversible voltage) is somewhat special to this application, and will be discussed in detail. There are several ways of treating surface potentials numerically. Here, we will focus on a method that solves the surface potential implicitly without requiring an extra fine mesh along the surface *S*. The basic idea is that the effective conductivity at surface *S* is calculated to ensure the correct surface potential. The current through face *A*, which is sketched in figure 1 and is a part of *S*, is conserved from one iteration to the next.

The following iterative procedure is applied to update the effective conductivity. It is written for a 2-dimensional non-orthogonal mesh like the one illustrated in figure 1.

The current through face *A* is expressed

$$jA \approx \int j_i dA_i = -\int \sigma_{eff} \frac{\partial \phi}{\partial \xi_k} \frac{\partial \xi_k}{\partial x_i} dA_i \approx \sigma_{eff} (\Delta\phi_1 Q_{11} + \Delta\phi_2 Q_{12}) \quad (6)$$

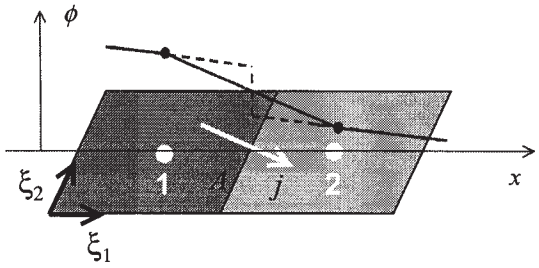

Figure 1: Sketch of two control volumes 1 and 2 with different electrical conductivity. Volume 1 belongs to the anode and volume 2 to the bath. The interface *A* is associated with a surface potential. The voltage is shown as a graph. The real shape of the curve is shown by the dashed line, while the solid line shows the discrete representation of the voltage. The local coordinate axes are ξ_1 and ξ_2, which are non-orthogonal.

where $\Delta\phi_1$ is the change of ϕ in the ξ_1 direction, and Q_{11} and Q_{12} are geometrical factors[1] taking into account the non-orthogonality of the mesh. Without overvoltage, σ_{eff} is the harmonic mean[2] of the electrical conductivity σ. When the face is associated with a surface potential,

$$\sigma_{eff} = \sigma_s \quad (7)$$

which is calculated to ensure the correct potential difference.

We assume that we can calculate the current through the surface potential face on the basis of the harmonic mean σ_h and an effective voltage gradient $\Delta\phi_{10}$ calculated from

$$\Delta\phi_1 = \Delta\phi_{10} + \phi_s . \quad (8)$$

The surface potential ϕ_s is given by eqs. (2-3) for the anode and (4) for the cathode in the present example. By applying eqs. (6-8) we can write the surface potential face current as

$$\sigma_s (\Delta\phi_1 Q_{11} + \Delta\phi_2 Q_{12}) = \sigma_h (\Delta\phi_{10} Q_{11} + \Delta\phi_2 Q_{12}) \quad (9)$$

where we have assumed that the ξ_2 direction is parallel to *S*. By rearranging (9), we can write an expression for the effective voltage difference:

$$\Delta\phi_{10} = \frac{\sigma_s}{\sigma_h} \Delta\phi_1 + \left(\frac{\sigma_s}{\sigma_h} - 1 \right) \frac{Q_{12}}{Q_{11}} \Delta\phi_2 \quad (10)$$

The surface potential effective conductivity σ_s is updated applying an iterative procedure based on conservation of face current from iteration ν to $\nu+1$. We express the current conservation

$$\sigma_s^{\nu+1} ([\Delta\phi_{10} + \phi_s] Q_{11} + \Delta\phi_2 Q_{12})^{\nu} = \sigma_s^{\nu} (\Delta\phi_1 Q_{11} + \Delta\phi_2 Q_{12})^{\nu} = (-jA)^{\nu} \quad (11)$$

which is rearranged to give an expression for σ_s. Initially, we apply

$$\sigma_s^{\,0} = \sigma_h \tag{12}$$

The procedure can be under-relaxed during the first few iterations to stabilise the calculations.

Bubble Trajectories

The coupling between the fluid dynamics and the electrodynamics is taken care of by a model that releases gas bubbles at the anode. The mass flow of gas (here in the case of oxygen) is proportional to the current:

$$\dot{n}_{O2} = \frac{jA}{4F} \qquad \text{[mol/s]} \tag{13}$$

where F is Faraday's constant.

The initial position of a single gas bubble is best explained with reference to figure 1. The mass center of the bubble is located in volume 2, at a distance corresponding to half the bubble diameter d_b away from the interface A between volumes 1 and 2. The number of initial bubble positions corresponds to the number of finite volumes on the bath side of the anode. The number of bubble trajectories calculated was either equal to the number (n_b) of initial positions, or to N*n_b in the case of turbulent dispersion, where N is large enough to ensure statistically independent results, see [3] for details.

The x-component of the equation of motion for a single bubble is

$$\frac{du_b}{dt} = (u - u_b)F_D + \frac{g_x(\rho_b - \rho)}{\rho_b} + \frac{F_v}{m_b} \tag{14}$$

Here, u_b is the bubble velocity, g is the acceleration of gravity, ρ is the density of fluid and gas (subscript b), m_b is the bubble mass, and the drag force term is

$$F_D = \frac{18\mu}{\rho_b d_b^{\,2}} \frac{C_D \mathrm{Re}}{24} \tag{15}$$

where μ is the dynamic viscosity of the bath and Re is the bubble Reynolds number. The drag coefficient C_D is dependent on the shape and velocity of the bubble relative to the surrounding bath. For small oxygen bubbles (1-3 mm) we apply a drag coefficient valid for solid spheres[3]. The last term in equation (14) is explained in the following section.

Wall potential model

When calculating bubble trajectories using the Lagrangian approach, the volumetric extent of the bubbles is not taken care of. This is a problem when the bubbles move close to a solid surface, such as the anode, because the bubble will be located within the finite volumes bounding the solid surface. The forces of the bubble-bath interaction will also be located in the finite volumes bounding the surface. Thus, the location of the forces is dependent on the specific subdivision of the cell geometry into finite volumes. The finer the mesh, the thinner the layer where the interaction takes place. In order to avoid this grid-dependency, we have implemented some changes in the Fluent code. These are:

- Generate a wall distance variable that varies smoothly
- Introduce a wall repelling, conservative force in the momentum equation for the bubbles
- Diffuse the momentum transfer from the bubbles to the bath over a region equivalent to the bubble volume

The distance from the walls (in this case the anode surface) r_w can easily be calculated in every position of the grid. Here, we have chosen to solve a Laplace equation with appropriate boundary conditions for r_v to obtain a smoothly varying approximation to the wall distance.

In order to make bubbles with finite size move away from walls, we introduce a potential that is a function of the wall distance. The wall potential is expressed:

$$\psi_v = -A_v \left[\frac{r_b}{r_v}\right]^n \tag{16}$$

Here, $r_b = d_b/2$ is the bubble radius, assuming a spherical shape, and A_v is a constant. It is not recommended to use a very hard potential; $n = 2$ was applied in the present calculations. The force is

$$F_v = -\nabla \psi_v \tag{17}$$

The constants of the model must be tuned to obtain plausible path lines of the bubbles, *i.e.* the centre-of-mass of the bubble should move at distance of approximately r_b away from the anode. The momentum is distributed around the point particle according to the discrete distribution function

$$p = \exp\left[-\frac{1}{2}\left[\frac{r}{r_b}\right]^2\right]\left\{\frac{\Delta\Omega}{\Delta\Omega_L}\right\} \tag{18}$$

Here, r is distance from point particle, $\Delta\Omega$ is the computational finite volume and $\Delta\Omega_L$ is computational finite volume where the point particle is located. The distribution must be properly normalised.

Two-way Coupling between Bubble Motion and Electric Field

The interaction between gas/bath motion and electric field is taken care of by eqs. (13) and (19), which is given below. The electrical conductivity is reduced due to the finite gas volume fraction in the bath. We apply the Brüggemann formula

$$\sigma = \sigma_{bath}(1 - \alpha_g)^{1.5} \tag{19}$$

where α_g is the volume fraction of gas.

Numerical Method and Solution Procedure

The solvers for the electromagnetic field and the wall distance have been added to the commercial CFD code Fluent 4.5 [3]. Fluent solves the Navier-Stokes equations for the bath convection, a Lagrange model for the discrete bubbles, which are modelled as particles, and an enthalpy equation for the heat transfer. We have applied a turbulence model for the bath turbulence (the so-called Renormalization Group k-ε model[3]). The electromagnetic field is solved simultaneously applying a multigrid solver.

Results

Heat Transfer at the Side-ledge in Hall-Heroult Cells

The heat transfer coefficient in Hall-Heroult cells is an important design factor, since the sidewalls must be protected by a frozen layer of cryolite. From a current efficiency point of view, the side channel should be as narrow as possible [5]; on the other hand, there is a risk that the protective side-ledge disappears due to the more intense gas induced convection.

The heat transfer coefficient between bath and side-ledge was calculated as a function of the width of the side channel for Søderberg cells as well as for prebake-cells. In an earlier work, a correlation for the heat transfer coefficient h_i at three different vertical positions along the side-ledge was derived [6]

$$h_i = C_i (Q \cdot 10^4 \cdot \alpha)^{ni}, \qquad i = 1,2,3 \qquad (20)$$

Here, C_i is a constant and α is the ratio between anode immersion depth and anode-ledge distance. Q is the gas flow rate per meter of periphery [$m^3 s^{-1} m^{-1}$]. Equation (20) is based on a recalculation of measurements made in a physical model. For comparison with the calculations, we have applied the mean value $h = \Sigma h_i/3$.

The gas flow rate into the side channel (Q) is approximately 4 times higher for Søderberg anodes than for prebaked anodes, but usually the anode – side ledge distance of the Søderberg cell is about twice that of the prebake - cell (approximately 0.2m). The bath height of Søderberg cells is also somewhat smaller than in the prebake-cell (approximately 20cm).

A comparison between the semi-empircal equation (20) and the Fluent calculations is given in figure 2. As can be observed, the results are in excellent agreement.

Flow and Current Distribution, Cell with Vertical, Inert Anodes

Calculations were performed for a two-dimensional aluminium electrolysis cell with vertical electrodes, as sketched in figure 3. The example has been chosen rather arbitrarily, with most of the parameters taken from traditional Hall-Heroult cells. In the absence of reliable overvoltage data for inert anodes, we select a = -0.67 and b = 0.2, in equation (3), which gives η_a = 0.1V for a current density j_a = 7000 A/m^2. We apply the constant $b_c = 2.4 \cdot 10^{-10}$ in Equation (4) and a reversible potential of 2.1V at the anode. The current efficiency was fixed at ε = 0.95 in the present calculations.

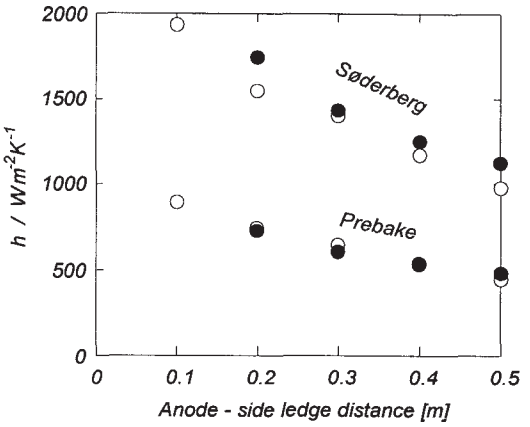

Figure 2: Heat transfer coefficient h [W/m^{2}K]from bath to side ledge. Filled symbols: Empirical, from Equation (20), open symbols: Fluent calculations.

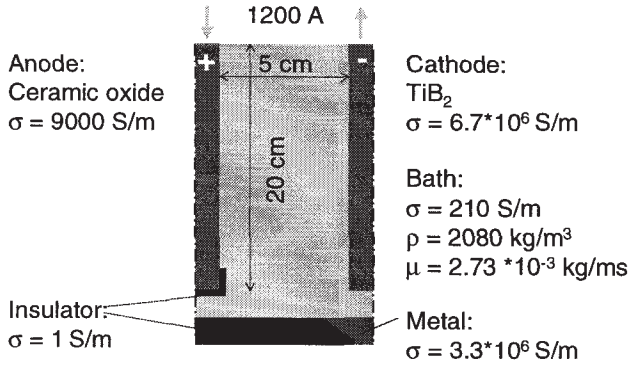

Figure 3: Geometry and parameters. The aspect ratio of the sketch is not correct. The depth of the model is 1 m.

Figure 4 shows that the overvoltage model predicts a considerable voltage drop at the anode surface, mainly due to the reversible potential. The electrical conductivity of the anode material is relatively low, so that the current density in the interpolar space decreases from the top of the anode and downwards. The bubble tracks were calculated applying a dispersion model[3] that takes into account the effect of turbulence on the bubble tracks. The bubble tracks are diverging from the anode surface due to the wall potential model described above. The amount of O_2 released is approximately 0.32 liters per second and meter of width at a gas density of 0.3 kg/m^3. The gas concentration, and thereby the reduction in electrical conductivity, is illustrated by the density of the track lines (see figure 4). The electrical conductivity was reduced from 210 S/m to approximately 150 S/m in the regions with the largest gas fraction.

The resulting convection pattern is shown to the right in figure 5 for a bubble size of 3mm. A main circulation and a small re-circulation zone are seen. In figure 6, the effect of bubble size is shown to be considerable. The small bubbles tend to rise close to

the anode, creating a narrow layer of high-speed bath, while larger bubbles distribute the forces over a thicker layer, thereby decreasing the peak bath velocity.

Discussion

In reality, bubble-bubble interaction will act partly as a repelling force and the bubbles will create turbulence in the bath due to the flow along the bubble contour. These effects are not taken care of with the present model. At high gas volume fractions (10% and higher), the Lagrangian model has the weakness that the interaction between gas and bath is only accounted for in the force balance and not in the mass balance. Future work should focus on the bubble characteristics of real systems and the proper modelling of the bubble-driven flow.

The low values of the cathodic overvoltage was a result of the choice of mass transfer model (5), which is better suited for free-surface flows than for flow along solid walls. By applying a relation for boundary layer flow, which results in a lower mass transfer coefficient, the cathodic overvoltage will increase.

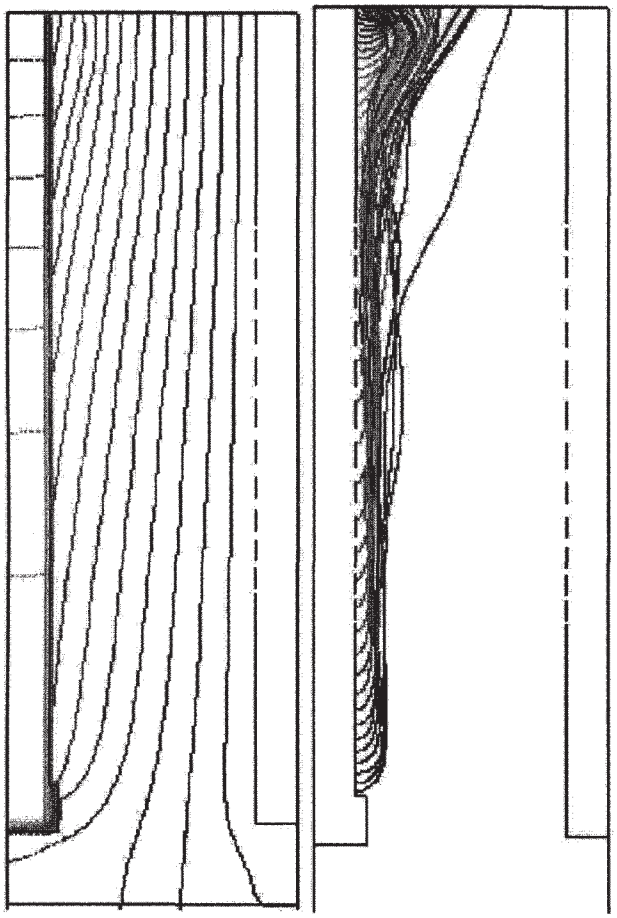

Figure 4: Electric potential (0-4.5 V) and resulting bubble tracks.

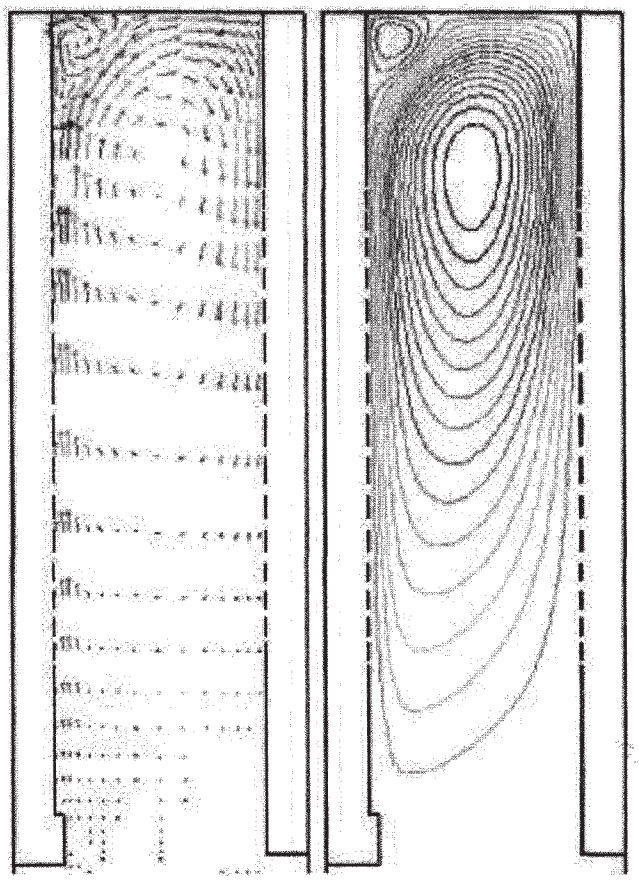

Figure 5: Bath velocity vectors (0 - 0.25 m/s) and streamlines. The bubble diameter is 3mm. The bottom of the cell is not shown.

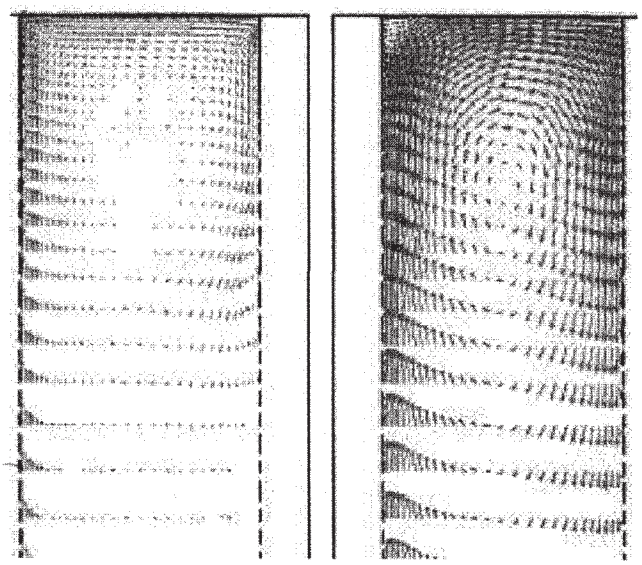

Figur 6: Bath convection pattern for 0.5mm (left) and 3mm bubble diameter. The maximum velocities are 0.46 m/s (left) and approx. 0.24 m/s (right). Only a part of the geometry is shown.

Concluding Remarks

Calculations of primary and secondary current distributions were coupled to anodic gas release and bath convection. The electrical conductivity was dependent on gas fraction. The equations were solved simultaneously to perform design calculations of an aluminium electrolysis cell with vertical, inert electrodes. The results show that the details of the convection pattern is strongly dependent on the bubble size. In another example, experimental data for the heat transfer coefficient at the side ledge were well predicted by the Fluent model for both Søderberg and prebake cells.

Acknowledgement

The present work is supported by the Norwegian aluminum industry, the Research Council of Norway and SINTEF Materials Technology. Permission to publish the results is gratefully acknowledged.

References

1. J. Ferziger and M. Peric, Computational methods for fluid dynamics, Springer 1997.
2. S.V. Patankar. Numerical heat transfer and fluid flow, Hemisphere 1980.
3. FLUENT 4.4 User's Guide, Fluent Inc, Lebanon, New Hampshire 1999.
4. V. de Angelis and S. Banerjee, Third international conference on Multiphase flow, Lyon, France June 8-12 1998.
5. A. Solheim and T. Haarberg, "A mechanistic approach to the prediction of current efficiency in industrial aluminium cells", Light Metals 2001
6. V.A. Khoklov, E.S. Filatov, A. Solheim & J. Thonstad, "Thermal conductivity in cryolitic melts - new data and its influence on heat transfer in aluminium cells", Light Metals 1998, pp. 501-505.
7. K. Grjotheim, C. Krohn, M. Maliniovsky, K. Matiasovsky, and J. Thonstad,, Aluminium Electrolysis, Aluminium-Verlag, Düsseldorf, 1982.
8. T. Haarberg, E. Olsen, A. Solheim, M. Dhainaut, P. Tetlie and S.T. Johansen, Bath-metal interfacial deformation due to gas induced flow in aluminium cells, Light Metals 2001.